Materials Characterization 169 (2020) 110656

Contents lists available at ScienceDirect

Materials Characterization

journal homepage: www.elsevier.com/locate/matchar

# EBSD analysis of hot deformation behavior of Cu-Ni-Co-Si-Cr alloy

YiJie Ban[a,b,c], Yi Zhang[a,b,c,*], Baohong Tian[a,b,c,*], KeXing Song[a,b,c,*], Meng Zhou[a,b,c,*], Xiaohui Zhang[a,b,c,*], Yanlin Jia[d], Xu Li[e], Yongfeng Geng[a,b,c], Yong Liu[a,b,c], Alex A. Volinsky[f]

[a] *School of Materials Science and Engineering, Henan University of Science and Technology, Luoyang 471023, PR China*
[b] *Provincial and Ministerial Co-construction of Collaborative Innovation Center for Non-ferrous Metal new Materials and Advanced Processing Technology, Henan Province, Luoyang 471023, PR China*
[c] *Henan Province Key Laboratory of Nonferrous Materials Science and Processing Technology, Luoyang 471023, PR China*
[d] *College of Materials Science and Engineering, Beijing University of Technology, Beijing 100124, PR China*
[e] *Center for Advanced Measurement Science, National Institute of Metrology, Beijing 100029, PR China*
[f] *Department of Mechanical Engineering, University of South Florida, Tampa 33620, USA*

## ARTICLE INFO

*Keywords:*
Cu-Ni-Co-Si-Cr alloy
Hot deformation behavior
Constitutive equation
Electron backscattered diffraction (EBSD)

## ABSTRACT

Cu-Ni-Si alloy is widely used in electronics industry due to its high electrical conductivity and high strength. In this paper, the Cu-Ni-Co-Si-Cr alloy is prepared by ZG-0.01 vacuum frequency induction melting furnace. The hot compression tests of the Cu-1.5Ni-1.1Co-0.65Si-0.2Cr alloy were carried out using the Gleeble-1500 simulator at 0.001–10 $s^{-1}$ strain rates and 500–900 °C deformation temperatures. The microstructure changes of the alloy at 500–900 °C were studied. The changes in the hot deformation process for the Cu-1.5Ni-1.1Co-0.65Si-0.2Cr alloy were analyzed by EBSD. The dislocation density was sacrificed to promote recrystallization. The DRX grains texture of the alloy at 700 °C is $\{001\} < 100 >$ cubic texture, which is replaced by the $\{011\} < 100 >$ Goss texture at 900 °C. And the higher deformation temperature makes the texture more random by lowering the texture intensity. The precipitates of the Cu-1.5Ni-1.1Co-0.65Si-0.2Cr alloy are mainly disk-shaped and rod-shaped $(Ni, Co)_2Si$. The constitutive equation of the Cu-1.5Ni-1.1Co-0.65Si-0.2Cr alloy was established to predict the behavior of the flow stress, and the activation energy is 634.45KJ/mol. Due to precipitation-hardened caused by $(Ni, Co)_2Si$, the activation energy of the Cu-1.5Ni-1.1Co-0.65Si-0.2Cr alloy was much higher than the self-diffusion activation energy of pure copper. And the CDRX and DDRX mechanisms are two dominant DRX mechanisms for the Cu-1.5Ni-1.1Co-0.65Si-0.2Cr alloy.

## 1. Introduction

Copper alloys are widely used in electronics industry, and as the inner wall of rocket engines and the first wall of nuclear reactors due to their high electrical conductivity and high strength [1–3]. At present, the Cu-Ni-Si alloy is one of the best alloy systems in terms of performance and processing. Commercial C70250 alloy (Cu-3.0Ni-0.65Si-0.15 Mg) shows high tensile strength of 600–850 MPa and medium electrical conductivity of 35–50%IACS (International Annealing Copper Standard). In order to further improve the strength of Cu-Ni-Si alloy, many scholars have added Co element into Cu-Ni-Si alloy. The addition of Co can form $Co_2Si$ precipitates, which can strength the alloy. In addition , Zhao et al. [4] reported a Cu-1.5 Ni-1.0Co-0.6Si alloy that had a microhardness of 250 HV and an electrical conductivity of 43% IACS. The addition of Co improves the strength of the alloy, but Co has a negative effect on the electrical conductivity of Cu-Ni-Si alloy. Therefore, the design of new copper alloy with high strength and electrical conductivity by adding some other elements has attracted much attention in recent years. The $Ni_2Si$ precipitates are found in Cu-Ni-Si alloys and can improve the strength of the alloy by precipitation hardening [4]. In recent decades, the addition of trace elements into the alloy systems has demonstrated improved electrical conductivity and strength of alloys. The addition of Co [5], Mg [6], Ag [7], Ti [8], V [9,10], Cr [11–14] can effectively improve the alloy strength. The addition of Co can form $Co_2Si$ precipitates, which can strength the alloy. The addition of Mg can decrease the stress relaxation of the Cu-Ni-Si alloys. The addition of Ti can effectively reduce the grain size and increase the grain elongation. The addition of V can inhibit the alloy recrystallization and promote the production of precipitates, which can improve hardness. The addition of Cr can improve the mechanical

---

[*] Corresponding authors at: School of Materials Science and Engineering, Henan University of Science and Technology, Luoyang 471023, PR China.
*E-mail addresses:* yizhang@haust.edu.cn (Y. Zhang), bhtian007@163.com (B. Tian), kxsong@mail.haust.edu.cn (K. Song), zhoumeng0902@126.com (M. Zhou), samuel0361@163.com (X. Zhang).

https://doi.org/10.1016/j.matchar.2020.110656
Received 6 May 2020; Received in revised form 27 August 2020; Accepted 16 September 2020

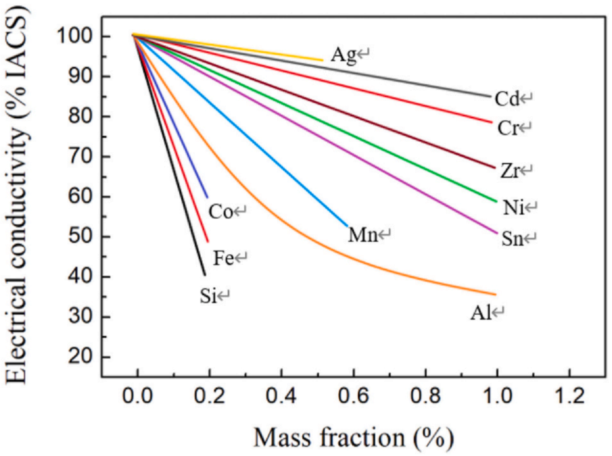

**Fig. 1.** The influence of different elements on the electrical conductivity of pure copper.

properties of the alloy, such as strength and hardness [15,16]. Noteworthy, the addition of Cr also has a positive effect on the physical properties. Wang et al. found that the thermal conductivity of copper matrix composites increased significantly by the Cr was added [17]. For the electrical conductivity, it can be seen from Fig. 1 that the Cr element has much less effect on the conductivity of the pure copper compared with some other elements. Besides, the Cr particles can precipitate from the copper matrix during aging at medium temperature, which improve the electrical property of alloy [18–20].

Hot deformation of materials is the basis of thermal processing, widely applied in manufacturing to improve the properties of alloys [21]. Lei et al. [22] investigated the hot compression behavior of Cu-Ni-Si alloy at 750–900 °C deformation temperatures and 0.001–1 $s^{-1}$ strain rates. It was found that the flow stress increased to a peak value and then decreased with increase of deformation time, which the continuous dynamic recrystallization behavior was shown, and the appropriate hot working temperature range was 850–875 °C. J. Chalon et al. [23] carried out the hot compression experiments on Cu-Ni-Si alloy at 600 °C, and found that the grains elongated and shear bands appeared. In order to take full advantage of the grain refining effects associated with dynamic recrystallization, the hot-working of the alloy should be carried out at temperatures above 800 °C. And previous studies of the Cu-Ni-Si alloy mainly focused on aging precipitation behavior, but few studies focused on the hot deformation behavior. Thus, the hot deformation behavior of the Cu-1.5Ni-1.1Co-0.65Si-0.2Cr alloy was investigated in this paper.

## 2. Experimental Procedure

The Cu-1.5Ni-1.1Co-0.65Si-0.2Cr alloy used in the experiment was cast in the ZG-0.01 vacuum frequency induction melting furnace at 1200 °C. High temperature resistant and oxidation-resistant graphite crucible was selected for melting. The size of graphite crucible is Φ 85 mm × 120 mm, and the maximum melting capacity is 10 kg. In order to prevent overflow during melting, the maximum melting capacity was 8.0 kg in this work. The raw materials were 99.95 wt% copper, pure Ni, Co, Si, and Cr. In order keep the chemical composition stable and minimize the impurity elements in the alloy, 0.05 MPa Ar gas was injected as a protective gas when the vacuum degree in the furnace chamber reached $10^{-3}$ MPa during smelting. Table 1 shows the actual compositions of the Cu-1.5Ni-1.1Co-0.65Si-0.2Cr alloy. After smelting, the ingots were annealed at 1000 °C for 1 h, and then extruded into 35 mm diameter bars by the XJ-500 metal profile extrusion machine. And then the extruded alloy was solution treated at 950 °C for 1 h in the KSS-1200 tubular resistance furnace, and argon was injected during this process. Then the samples were machined into Φ8 mm × 12 mm cylinders for hot compression testing. After the preparation work was completed, the hot compression tests were conducted using the Gleeble-1500D thermo-mechanical simulator. The temperature was set at 500–900 °C and the strain rate was 0.001–10 $s^{-1}$. During this process, the samples were heated to the target temperature at 10 °C/s heating rate and then kept at this temperature for 3 min. The compression of the samples was 55%.

**Table 1**
The nominal and analyzed composition of the Cu-1.5Ni-1.1Co-0.65Si-0.2Cr alloy.

| Nominal composition (wt%) | Analyzed composition (wt%) | | | | |
|---|---|---|---|---|---|
| | Ni | Co | Si | Cr | Cu |
| Cu-1.5Ni-1.1Co-0.65Si-0.2Cr | 1.452 | 1.065 | 0.630 | 0.195 | Bal. |

After the tests, the specimens were cut along the longitudinal plane to analyze the microstructure evolution of the Cu-1.5Ni-1.1Co-0.65Si-0.2Cr alloy. The specimens were etched in the solution (5 g $FeCl_3$, 10 mL HCl, 100 mL distilled water), and the microstructure was observed by the OLYMPUS PMG3 optical microscope. The EBSD images were obtained by using the JMS-7800F field emission scanning electron microscope (SEM) with a step size of 0.5 um and a voltage of 20 KV. The software Transmission Channel 5 was used to analyze the EBSD data. The specimens were electropolished in a solution containing 50% alcohol and 50% phosphoric acid at 20 °C and 5 V. The TEM images were obtained by using the JEM-2100F transmission electron microscope operated at 200 kV. The specimen was processed into a wafer with a thickness of 50 um and a diameter of 3 mm, and subsequently ion thinned by using Gatan 691 ion beams thinner.

In this work, hot compression experiments with the Cu-1.5Ni-1.1Co-0.65Si-0.2Cr alloy were carried out at the deformation temperature of 500–900 °C and the strain rate of 0.001–10 $s^{-1}$ by the Gleeble-1500 thermo-mechanical simulator. The true stress-true strain curves of the alloy were obtained. The microstructure of the alloy was analyzed by an optical microscope. The dislocation density and texture of the alloy at different conditions were obtained by electron backscatter diffraction (EBSD), and the precipitates were observed by transmission electron microscopy (TEM).

## 3. Results

### 3.1. True Stress–True Strain Curves

Fig. 2 shows the true stress-true strain curves of the Cu-1.5Ni-1.1Co-0.65Si-0.2Cr alloy. The stress increased rapidly to the peak value during hot compression, which is a typical feature of work hardening. During the work hardening stage, the slip surface and the lattice are distorted, and dislocations are entangled with strong interactions. At this time, the strength of the material increases significantly, but the further processing of the material can be hindered due to the decrease of plasticity. It is worth noting that the deformation temperature and rate significantly affect the true stress-true strain curves. At lower temperature and higher strain rate, the peak stress value is higher due to a large number of dislocations entangled in this condition, leading to restricted dislocations motion. In general, the flow stress was first promptly increased to peak stress at the beginning of compression, and then decrease to a steady state. It was noticed that the obvious downward tendency was observed at low temperature (500 °C and 600 °C), which indicated that the dynamic softening effect exceeds the work hardening effect. Dynamic softening includes dynamic recovery (DRV) and dynamic recrystallization (DRX) The occurrence of DRV means that the dislocations in the alloy canceled out and rearranged, which reduced the residual stress in the alloy and improved plasticity and toughness. The DRX reduced the residual stress in the alloy by

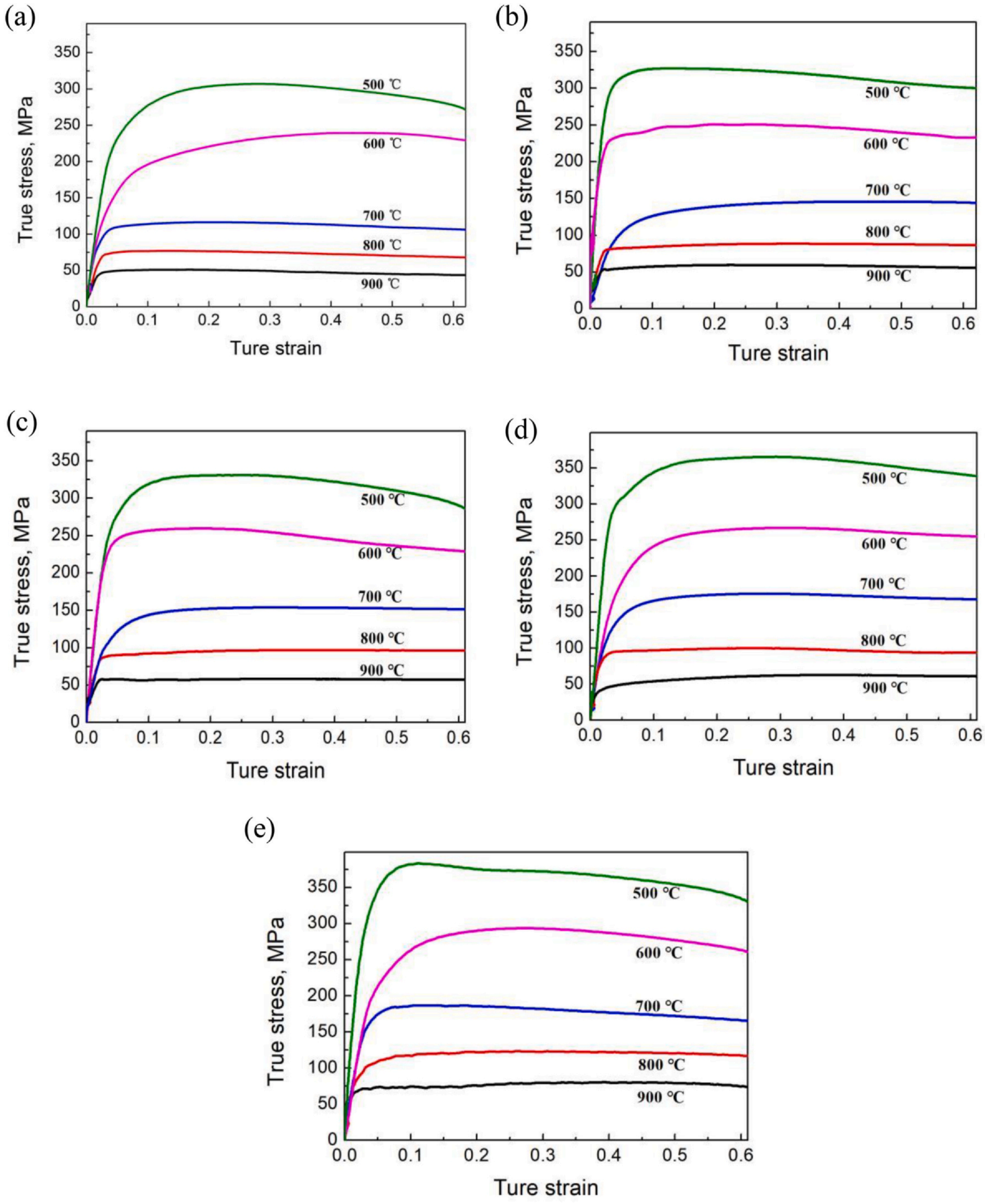

**Fig. 2.** True stress-true strain curves of the Cu-1.5Ni-1.1Co-0.65Si-0.2Cr alloy deformed at different temperatures and strain rates: (a) 0.001 $s^{-1}$; (b) 0.01 $s^{-1}$; (c) 0.1 $s^{-1}$; (d) 1 $s^{-1}$; (e) 10 $s^{-1}$.

producing new grains. Dynamic softening and work hardening can make the stress value of the alloy reach equilibrium at 700–900 °C [24,25]. DRX mechanism can be divided into continuous DRX (CDRX) and discontinuous DRX (DDRX). The nucleation mechanism of DDRX is nucleated by grain boundary bugging, and the main nucleation mechanism of CDRX is nucleated by sub-grain rotation. [26–30]. In the whole process of hot deformation, work hardening and dynamic softening compete. In the early stage of hot deformation, work hardening plays a major role in increasing the stress value, but the rate of this increase gradually decreases. When the peak stress is reached, dynamic softening can overcome work hardening, keeping a relative balance between them [31].

### 3.2. *Constitutive Equation*

The constitutive equation, proposed by Sellars and McTegart [32], is widely used to describe the relationship between the peak stress ($\sigma$), deformation temperature ($T$), and strain rate ($\dot{\varepsilon}$) in the process of hot deformation [33]. It can be expressed as follows:

$$\dot{\varepsilon} = A\left[\sinh(\alpha\sigma)\right]^{n} exp\left[-\frac{Q}{RT}\right] \text{(For all)} \tag{1}$$

Generally, the hyperbolic sine function in the Arrhenius equation can be simplified into exponential and power functions under the condition of low stress and high stress:

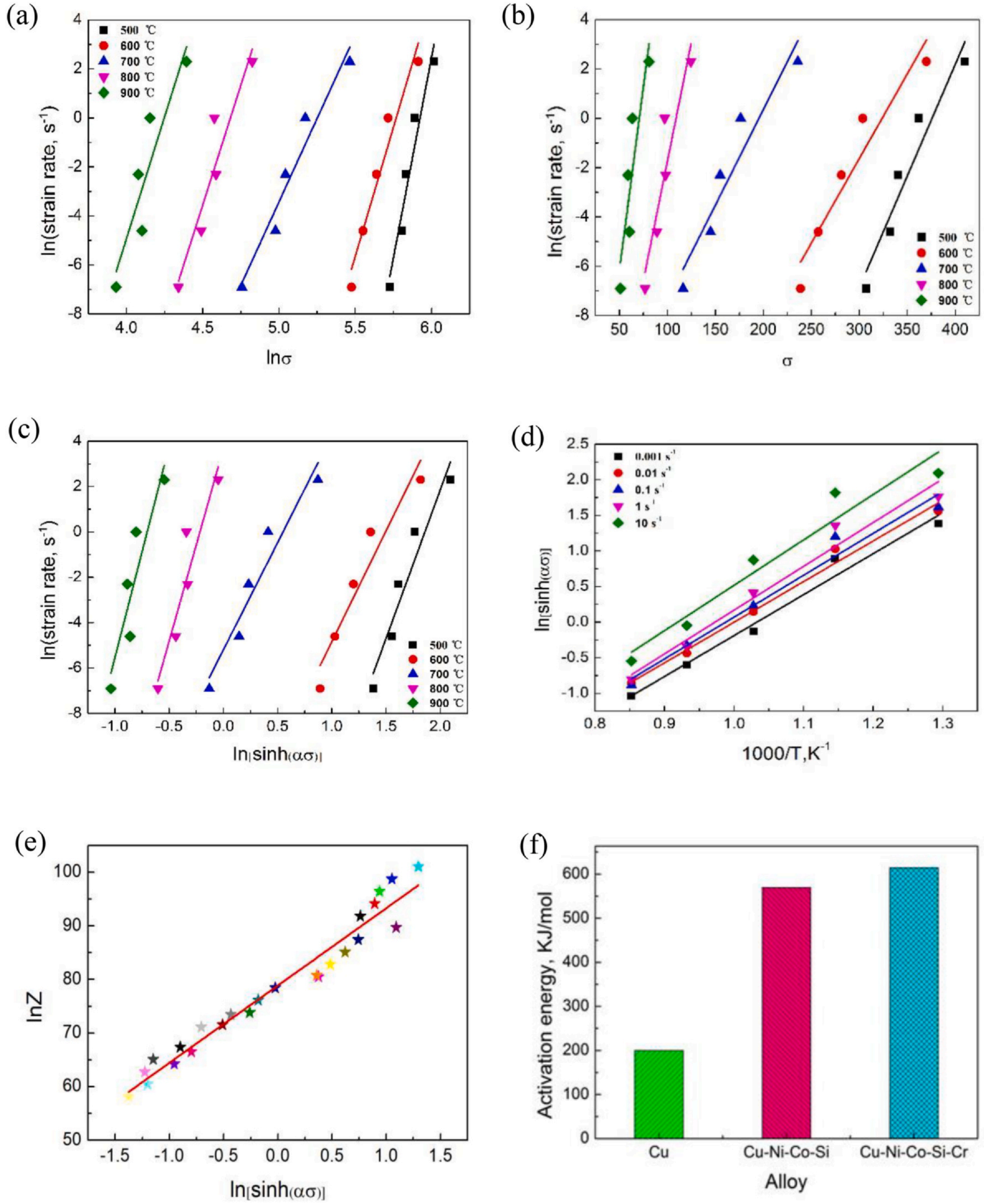

**Fig. 3.** Relations between: (a) ln $\dot{\varepsilon}$ - ln σ; (b) ln $\dot{\varepsilon}$ - σ; (c) ln $\dot{\varepsilon}$ - ln[sinhασ]; (d) ln[sinhασ] - 1000/T; (e) ln Z - ln[sinhασ]; (f) deformation activation energy of the Cu, Cu-Ni-Co-Si and Cu-Ni-Co-Si-Cr alloys.

$$\dot{\varepsilon} = A_1\sigma^{n_1} exp\left[-\frac{Q}{RT}\right] \alpha\sigma < 0.8 \tag{2}$$

$$\dot{\varepsilon} = A_2 \exp(\beta\sigma)\, exp\left[-\frac{Q}{RT}\right] \alpha\sigma > 1.2 \tag{3}$$

Here, $A$, $A_1$, $A_2$, and $n_1$ are material constants, $n$ is the stress exponent, and $\alpha$ is the stress multiplier. It should be noted that $\sigma$ was considered as the peak stress due to the difficulty of attaining steady-state at high strain rates. At the low stress level ($\alpha\sigma < 0.8$) and high stress level ($\alpha\sigma > 1.2$), the strain rate could be described in Eqs. (2) and (3), respectively.

The Zener-Hollomon parameter (the $Z$ parameter) proposed by Zener and Hollomon [34–36] was used to express the effects of temperature and deformation rate on the flow behavior:

$$Z = \dot{\varepsilon}\, exp\left[\frac{Q}{RT}\right] = A[\sinh(\alpha\sigma)]^n \tag{4}$$

Here, $Q$ is the thermal activation energy (J/mol), $R$ is the universal gas constant ($R$ = 8.31 J/mol·K), $n_1$, $b$, and $n$ are the material constants. To simplify these equations, taking the natural logarithm of both sides of Eqs. (1)-(3) yields:

$$\ln\dot{\varepsilon} = n\ln[\sinh(\alpha\sigma)] - \frac{Q}{RT} + \ln A \tag{5}$$

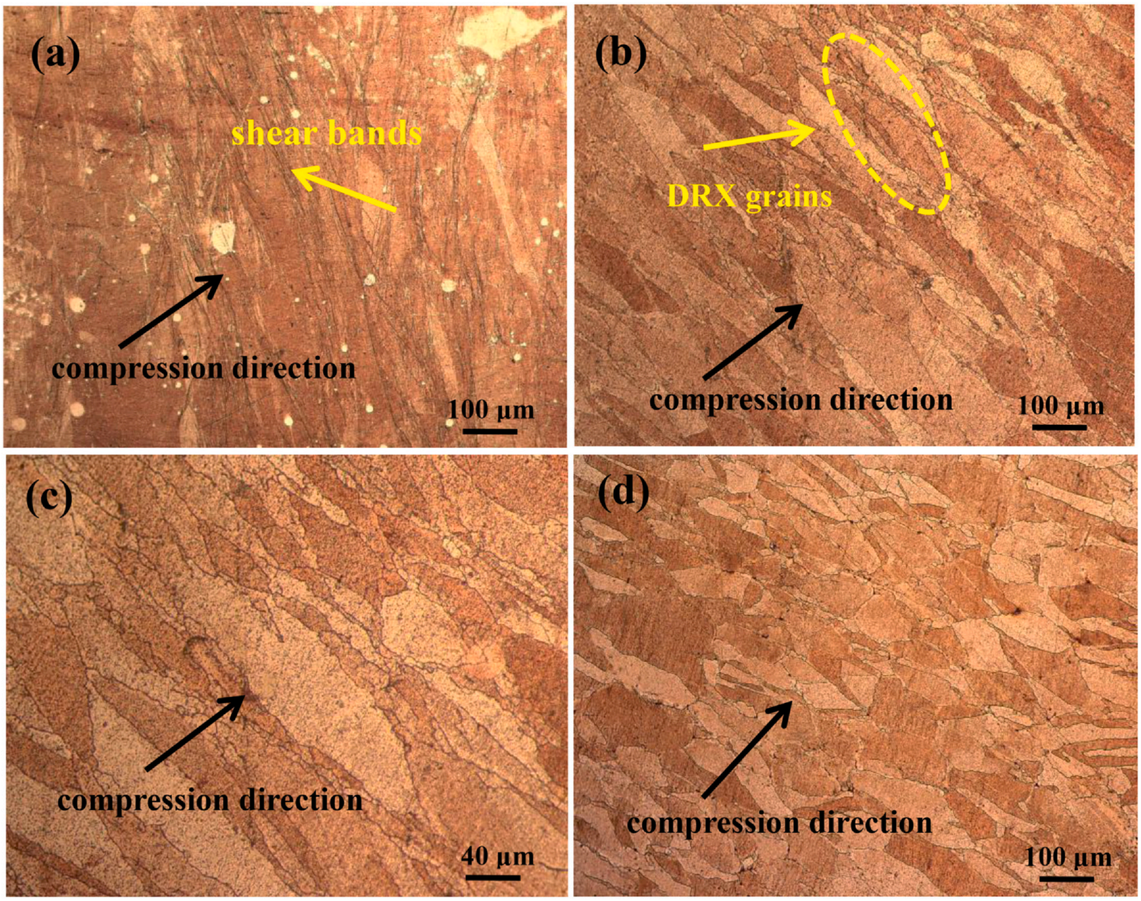

**Fig. 4.** Optical images of the Cu-1.5Ni-1.1Co-0.65Si-0.2Cr alloy microstructure under different hot deformation conditions: (a) 500 °C and 0.01 $s^{-1}$; (b) 700 °C and 0.01 $s^{-1}$; (c) magnification of DRX grains in (b); (d) 900 °C and 0.01 $s^{-1}$.

$$\ln \dot{\varepsilon} = n_1 \ln \sigma + \ln A_1 - \frac{Q}{RT} \tag{6}$$

$$\ln \dot{\varepsilon} = \beta\sigma + \ln A_2 - \frac{Q}{RT} \tag{7}$$

Eqs. (6) and (7) can be partially differentiated to obtain $n_1 = \frac{\partial \ln \dot{\varepsilon}}{\partial \ln \sigma}$ and $\beta = \frac{\partial \ln \dot{\varepsilon}}{\partial \sigma}$. Therefore, a linear relation can be obtained for ln(strain rate) - ln$\sigma$ and ln(strain rate) - $\sigma$, which was shown in Fig. 3(a) and (b), respectively. The value of $\beta$ was determined at high stress, which was the average value at 500–600 °C deformation temperature: $\beta = 0.080$. The value of $n_1$ was determined at low stress, which was the average value at 700–900 °C deformation temperature: $n_1 = 16.693$. Thus, the stress multiplier value $\alpha$ was determined as 0.0049, according to $\alpha = \beta / n_1$.

Activation energy $Q$ is a measure of the minimum energy required to stimulate dislocation movement by diffusion [37]. It is regarded as an important physical parameter to reflect the degree of difficulty of the material deformation under various conditions [38]. The deformation activation energy ($Q$) can be determined from Eq. (8):

$$Q = R\left[\frac{\partial \ln \dot{\varepsilon}}{\partial \ln[\sinh(\alpha\sigma)]}\right]_T \left[\frac{\partial \ln[\sinh(\alpha\sigma)]}{\partial (1/T)}\right]_{\dot{\varepsilon}} = RnS \tag{8}$$

Here, $n$ is the average of the slopes of ln$\dot{\varepsilon}$ - ln[sinh$\alpha\sigma$] in Fig. 3(c). $S$ is the average of the slopes of ln[sinh$\alpha\sigma$] - 1000/T in Fig. 3(d). Thus, $n$ and $S$ were determined as 14.976 and 5.108, respectively. The activation energy of the Cu-1.5Ni-1.1Co-0.65Si-0.2Cr alloy can be calculated as 634.45 KJ/mol from Eq. (8).

Fig. 3(e) shows a linear relationship between lnZ - ln[sinh$\alpha\sigma$]. Taking natural logarithms on both sides of Eq. (8) yields:

$$\ln Z = \ln A + n \ln[\sinh(\alpha\sigma)] \tag{9}$$

ln$A$ is the intercept of Fig. 3(e), which can be obtained as ln$A$ = 78.83. Therefore, the value of $A$ could be obtained as $A = e^{78.83}$. According to the above values, the constitutive equations for the Cu-1.5Ni-1.1Co-0.65Si-0.2Cr can be expressed as follows:

$$\dot{\varepsilon} = e^{78.83}[\sinh(0.0049)]^{14.98} exp\left(-\frac{634.45}{RT}\right)$$

Fig. 3(f) shows the activation energy of Cu [39], Cu-Ni-Co-Si [40] and Cu-Ni-Co-Si-Cr alloys. The activation energy of pure copper is much lower than the other two alloys. This means that the Cu-Ni-Co-Si and Cu-Ni-Co-Si-Cr alloys have better high-temperature stability. Moreover, the addition of Cr increased the activation energy of the Cu-Ni-Co-Si-Cr alloy by 8.2% compared with the Cu-Ni-Co-Si alloy.

### 3.3. Microstructure Evolution

Fig. 4 shows microstructure of the Cu-1.5Ni-1.1Co-0.65Si-0.2Cr alloy deformed at different conditions. Fig. 4(a) shows microstructure of the alloy deformed at 500 °C and 0.01 $s^{-1}$, where only elongated and distorted grains can be observed, and the heat generated by local deformation cannot transfer to other parts rapidly, resulting in non-uniform distribution of temperature and flow localization. When the temperature reached recrystallization condition, dynamic recrystallized grains were formed, as seen in Fig. 4(b). Dynamic recrystallization occurs preferentially at the grain boundaries because their energy is higher than inside the grain, providing the driving force for dynamic recrystallization. Fig. 4(c) is the enlarged region of Fig. 4(b), where dynamic recrystallized grains with an average size of 5.3 μm can be

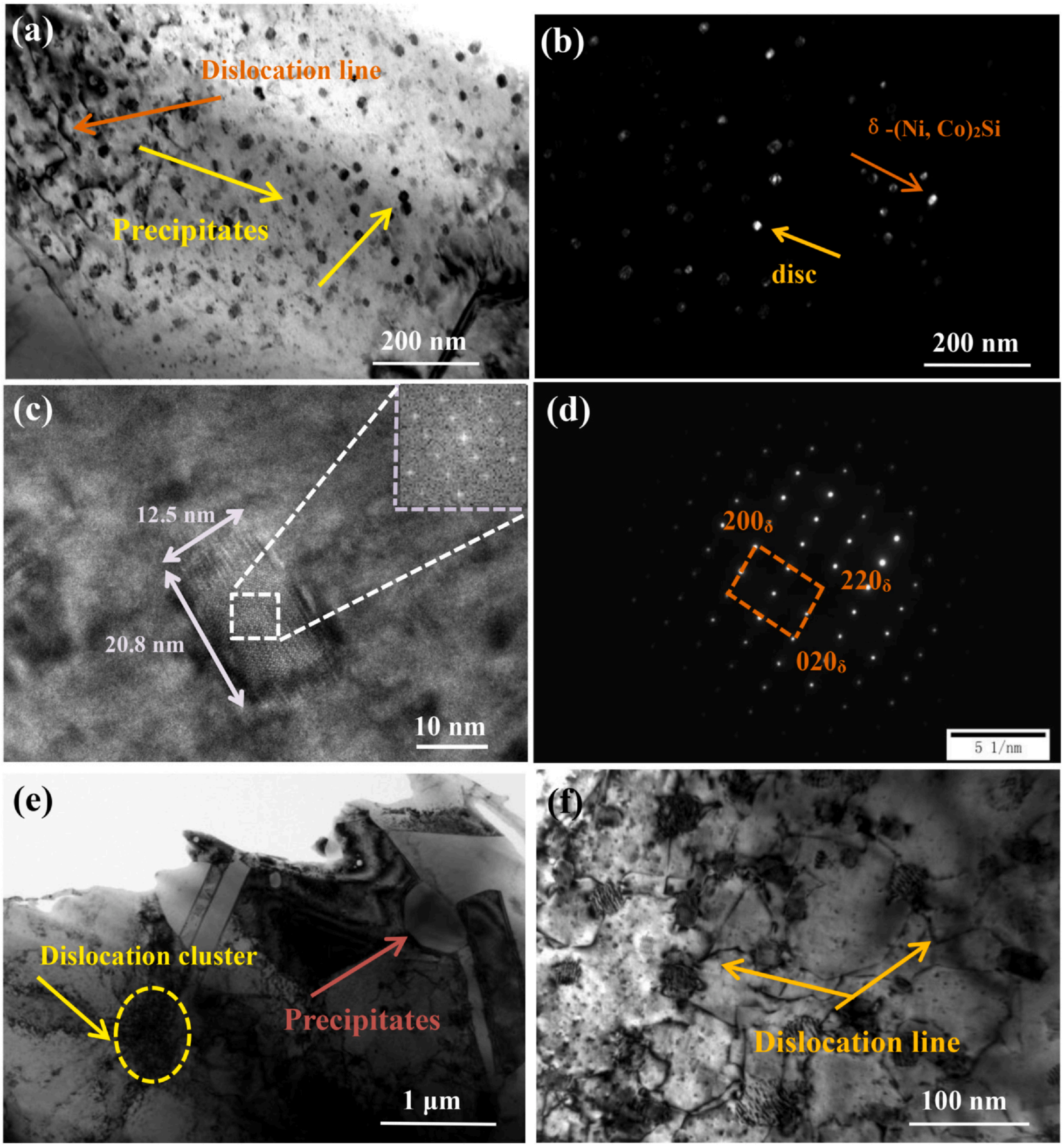

**Fig. 5.** Microstructure of the Cu-1.5Ni-1.1Co-0.65Si-0.2Cr alloy deformed at 0.001 $s^{-1}$ and 700: (a) bright-field micrograph; (b) dark-field micrograph of (a); (c) HRTEM of the δ-(Ni, Co)$_2$Si; (d) SADP of (Ni, Co)$_2$Si; (e) and (f) bright field TEM image.

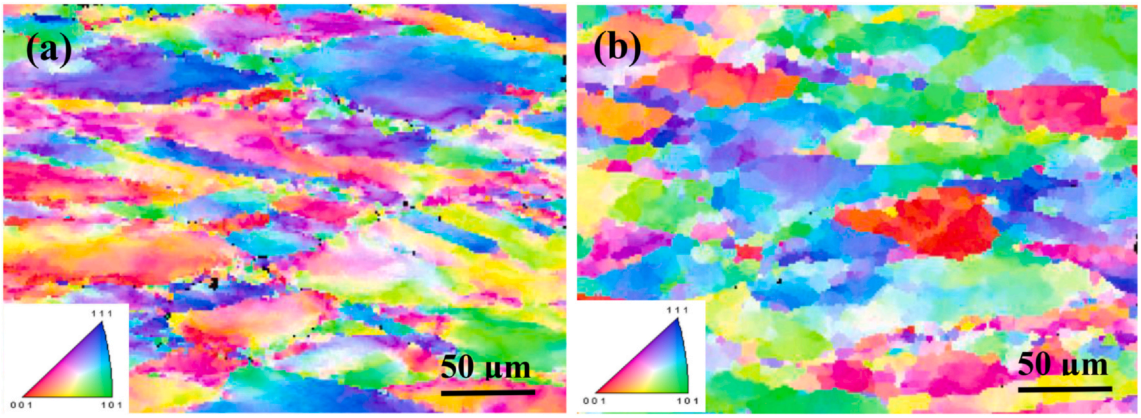

**Fig. 6.** EBSD micrographs of the Cu-1.5Ni-1.1Co-0.65Si-0.2Cr alloy deformed at: (a) 700 °C and 0.001 $s^{-1}$, (b) 900 °C and 0.001.

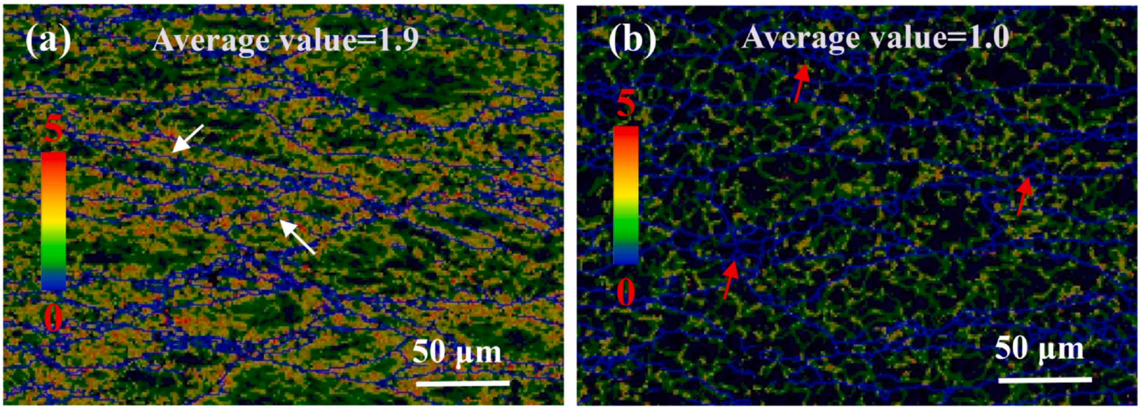

**Fig. 7.** The Kernel Average Misorientation (KAM) of the Cu-1.5Ni-1.1Co-0.65Si-0.2Cr alloy deformed at: (a) 700 °C and 0.001 $s^{-1}$; (b) 900 °C and 0.001 $s^{-1}$.

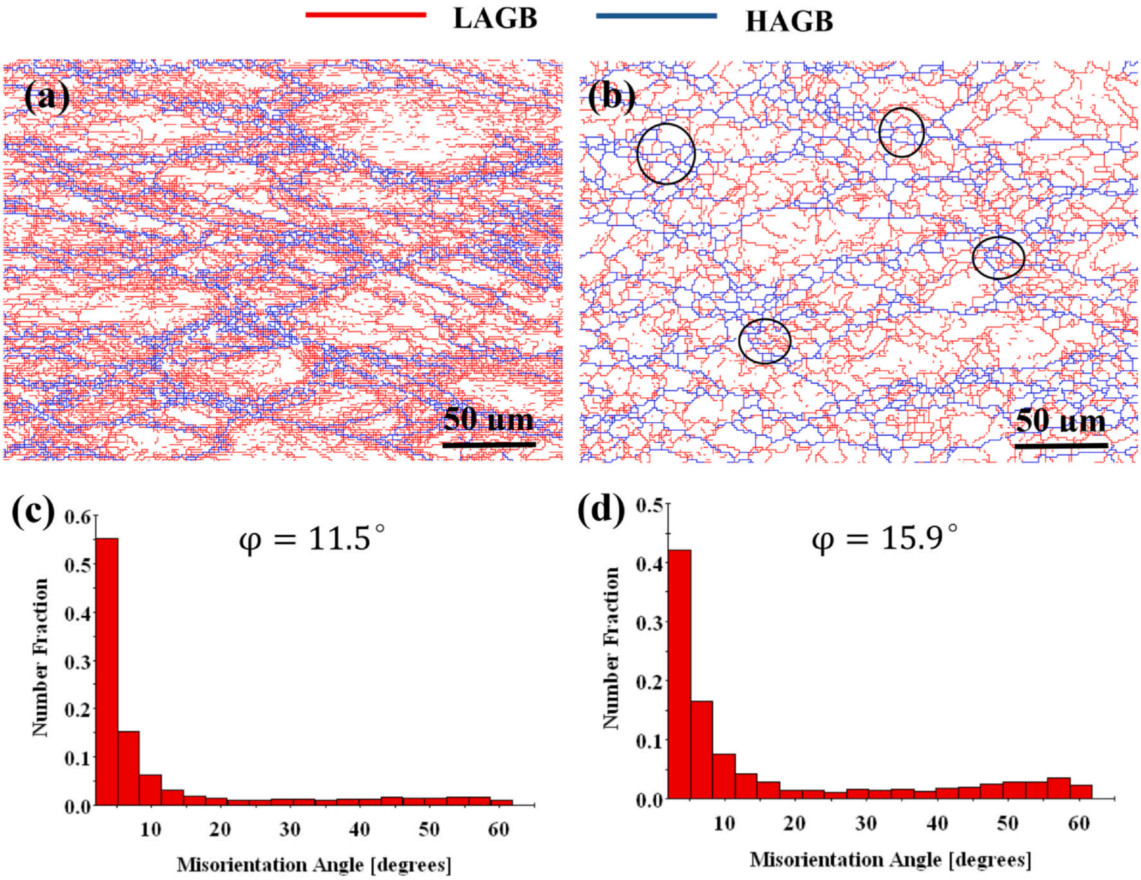

**Fig. 8.** Orientation maps and misorientation angle distributions of the Cu-1.5Ni-1.1Co-0.65Si-0.2Cr alloy deformed at: (a) and (c) 700 °C,0.001 $s^{-1}$; (b) and (d) 900 °C, 0.001 $s^{-1}$. HAGBs are shown as blue lines, and LAGBs are shown as red lines. (For interpretation of the references to color in this figure legend, the reader is referred to the web version of this article.)

clearly seen. With the increase of hot deformation temperature in Fig. 4(d), more recrystallized grains appear and replace the original grains [41]. With the recrystallization, the internal stress is eliminated. In addition, uniform recrystallization structure replaces the original coarse structure, and the refinement of the grains increases the alloy strength [42].

### 3.4. Precipitates

Fig. 5 shows transmission electron microscopy (TEM) micrographs of the Cu-1.5Ni-1.1Co-0.65Si-0.2Cr alloy deformed at 700 °C and 0.001 $s^{-1}$. There are many precipitates with the 15–25 nm size in Fig. 5(a), and the precipitates exist on the dislocation line, which hinders dislocations movement and improves the resistance to plastic deformation. Fig. 5(b) shows the dark-field TEM micrograph of Fig. 5(a). There are two kinds of precipitates with different shapes, which can be divided into disc-shaped and rod-shaped. It has been proven that the disc-shaped precipitated phase is δ-$Ni_2Si$ by Jia et al. research results [43]. When the δ-$Ni_2Si$ is parallel to the beam, it becomes rod-shaped. In the experiment, a part of the Ni atoms in the $Ni_2Si$ phase will be replaced by Co atoms, forming $(Ni, Co)_2Si$. Since Ni and Co have close lattice parameters, $Ni_2Si$ has orthorhombic structure with a = 0.708 nm, b = 0.490 nm and c = 0.373 nm, Pbnm (62) [44], while the lattice parameters of $Co_2Si$ are a = 0.710 nm, b = 0.491 nm, and

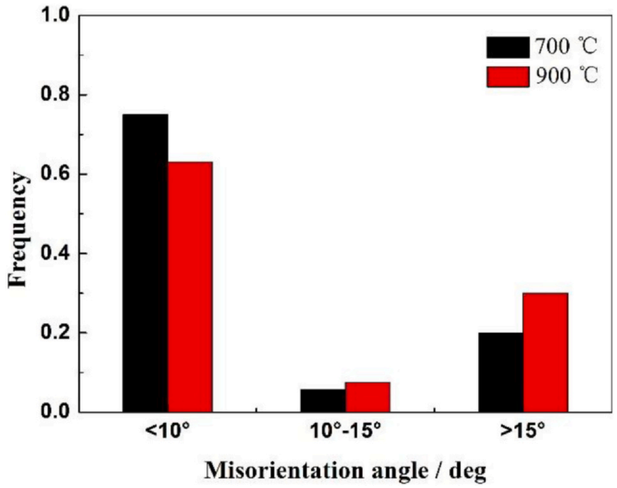

**Fig. 9.** Variations of misorientation angle scopes with deformation temperature.

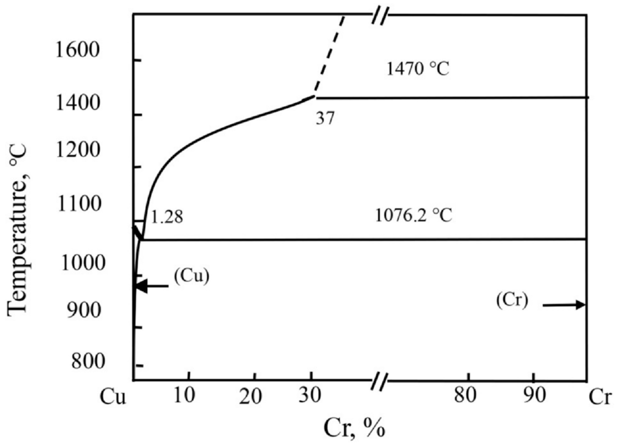

**Fig. 10.** Cu−Cr phase diagram.

c = 0.377 nm [45]. Therefore, it is believed that the precipitates mainly exist in the form of (Ni, Co)$_2$Si.

Fig. 5(c) shows high-resolution TEM (HRETEM) micrograph and the corresponding fast Fourier transform (FFT) pattern of the rod-like shaped precipitate, and Fig. 5(d) shows the small area diffraction pattern (SADP) of the precipitate in Fig. 5(c), which also proves that the precipitate is (Ni, Co)$_2$Si. Fig. 5(e) shows the position of precipitates, where precipitates at the grain boundaries coarsen, so their size (436.7 nm) is much larger than the precipitates inside the grain (average size is 21.4 nm). During hot compression, localized flow accelerated precipitation coarsening in the sheared area. It should be noted that this situation would lead to cavity growth at the shear band, which will result in specimen fracture upon higher strain [46]. In addition, according to Fig. 5(e) and (f), fine precipitates pin dislocations and a large number of dislocations gather to form dislocation cells, which can improve the alloy strength.

### 3.5. EBSD

Fig. 6 shows EBSD images of the Cu-1.5Ni-1.1Co-0.65Si-0.2Cr alloy deformed at 700 °C, 0.001 s$^{-1}$ and 900 °C, 0.001 s$^{-1}$, respectively. The original grains of the alloy have been elongated, accompanied by the formation of fine dynamically recrystallized grains at 700 °C, and the average recrystallized grain size was 4.3 μm. so the original structure was substituted by the dynamically recrystallized grains with increased temperature.

Fig. 7 shows the dislocation density of the Cu-1.5Ni-1.1Co-0.65Si-0.2Cr alloy at 700 °C and 900 °C, respectively. In the process of hot deformation, the migration of grain boundaries has a great influence on dynamic recrystallization, and the migration of grain boundaries is associated with the dislocations near the grain boundaries. The dislocation density change and distribution can be obtained from the Kernel Average Misorientation (KAM) maps. According to the low dislocation density (the region marked by blue color) and the highest dislocation density (the region marked by red color), it is found that the dislocation density at 700 °C is much higher than that at 900 °C, which also indicates that the occurrence and coarsening of DRX sacrifice dislocations [47]. In addition, it is found that the high dislocation density is mainly concentrated near the grain boundary, and the dislocation density inside the grain is much lower than at the grain boundaries. This situation can be clearly seen in Fig. 7(a), which also explains the reason why dynamic recrystallization occurs preferentially at the grain boundaries.

Fig. 8 shows the orientation maps and misorientation angle of the Cu-1.5Ni-1.1Co-0.65Si-0.2Cr alloy, respectively. There are many low angle grain boundaries (LAGBs, < 10°) at low temperature in Fig. 8(a), which results in aggregation of dislocations in the deformed grain boundaries and work hardening regions. With the increase of temperature, LAGBs are transformed into high angle grain boundaries (HAGBs) through the rotation of sub-grains and the growth of recrystallized grains. The average misorientation angle increased from 11.5° to 15.9° in Fig. 8(c) and (d). When the grain misorientation value of both sides of the grain boundary is small, the migration velocity of the grain boundaries is smaller. The orientation difference between the grains increases with the degree of recrystallization. The percentage of high angle grain boundaries (HAGBs) increases from 19.2% to 29.3% with temperature. This means that with the increase of HAGBs, the degree of recrystallization is further improved [48].

## 4. Discussion

### 4.1. DRX Mechanism

The new grains with HAGBs were observed in the EBSD images, indicating that DRX occurred during hot deformation. DRX mechanism can be divided into continuous DRX (CDRX) and discontinuous DRX (DDRX) [49,50]. For CDRX, the dislocations produced by plastic deformation gradually accumulate in LAGBs, leading to misorientaion increasing and the formation of HAGBs. In contrast, during DDRX, new grains result from the generation of recrystallization nuclei (new strain-free grains with HAGBs) and the subsequent long-range migration of their boundaries at the expense of stored energy.

It can be seen that some nuclei marked with black circles in Fig. 8(b) have formed HAGBs but still with partial LAGBs, which proves that the new grains may be formed by CDRX [51,52]. In addition, CDRX is characterized by the progressive sub-grain rotation, and hence the occurrence of CDRX must be accompanied by the transformation from LAGBs to HAGBs [53]. An increased fraction of 10–15° GBs was found to feature this transformation process [54,55]. Fig. 9 shows the variations of misorientation angle scopes with deformation temperature. It can be seen that the fraction of 10–15° misorientations increases from 5.7% to 7.4% with the increase of temperature, implying that the sub-grain rotation is the DRX mechanism.

Obvious serrating and bulging (marked by white arrows) at the original grain boundary can be observed from Fig. 7(a), and all these serrated GBs were accompanied by high KAM regions. It indicated that the DDRX characterized by grain boundary bulging was activated here. When the deformation temperature is 900 °C (Fig. 7(b)), the newly formed strain-free DRX grains (marked by red arrows) were observed around initial HAGBs, which is a powerful evidence of DDRX occurrence [56,57].

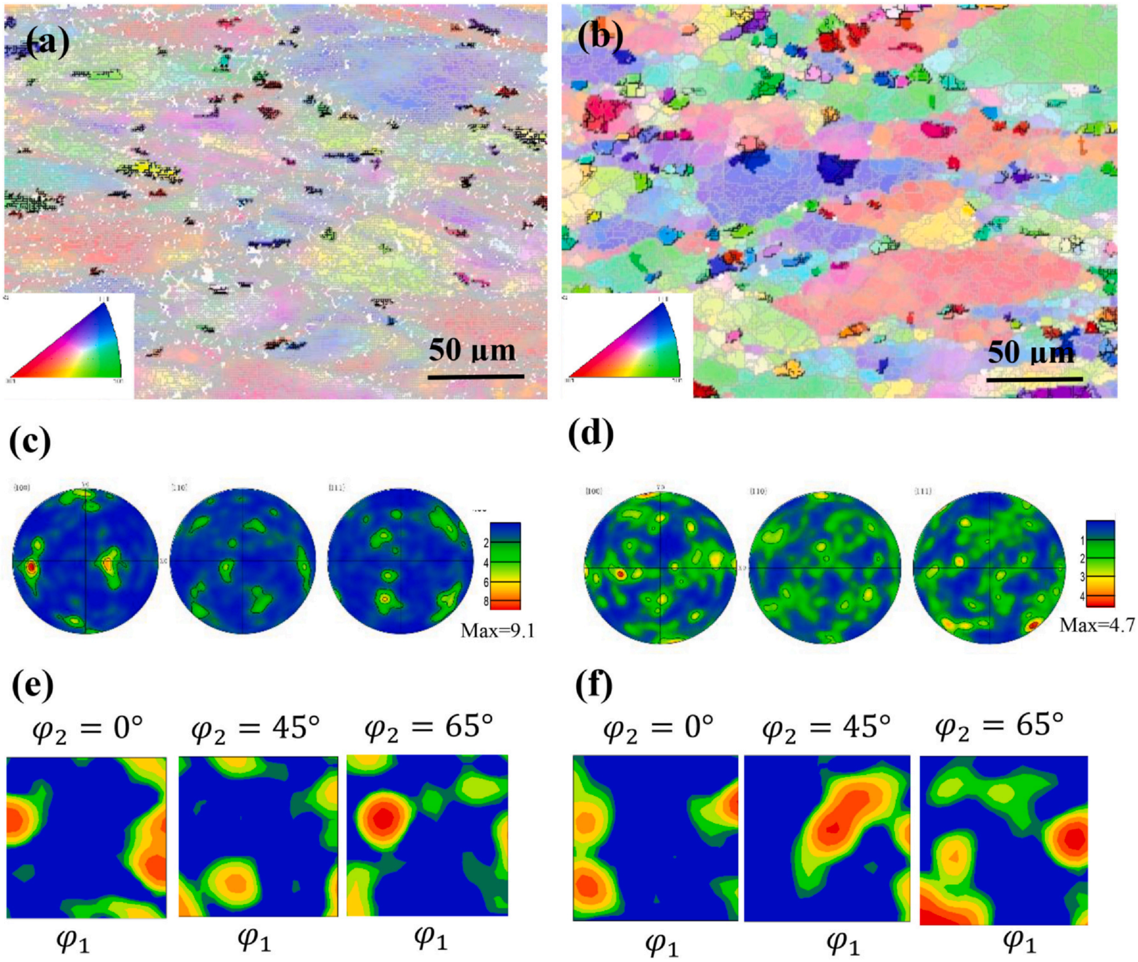

**Fig. 11.** DRXed-grains EBSD images, DRXed-grains pole figure and DRXed-grains ODF maps of the Cu-1.5Ni-1.1Co-0.65Si-0.2Cr alloy: (a), (c) and (e) 700 °C, 0.001 $s^{-1}$, (b), (d) and (f) 900 °C, 0.001 $s^{-1}$.

### 4.2. Activation Energy

In the present study, the activation energy of the alloy was 634.45 kJ/mol during hot compression, which was much higher than the self-diffusion energy of pure copper (203.6 kJ/mol) [39]. The stress exponent $n$ value in this experiment is 14.98, which is higher than those ($n = 5$ or $n = 3$) in alloys deformed by a dislocation-climb or a dislocation-glide mechanism, respectively [58]. A high $n$ value is usually indicative the main strengthening mechanism is precipitation-hardened mechanism [59], It also showed that the precipitates in the matrix that impede the movement of dislocations, consequently producing a high stress exponent in these types of alloys. The deformation of the alloy is controlled by the viscous glide of dislocations. Li et al. [60,61] also verified this view.

Remarkably, compared with our previous work on the Cu-Ni-Co-Si alloy [40], the addition of Cr increased the activation energy of the Cu-Ni-Co-Si alloy by 8.2%. The main reason is that the addition of Cr made more $(Ni, Co)_2Si$ precipitates during the hot deformation process, increasing from 15.7% to 27.3%. More precipitates pin the grain boundaries and dislocations, finally leading to the activation energy increase [62–64]. No Cr-containing precipitates were found here, mainly due to Cr dissolved into the Cu-matrix in the solid solution stage, according to the Cu−Cr phase diagram (Fig. 10), the solubility of Cr in Cu-matrix at 1000 °C is 0.65%, and the low Cr content (mass fraction 0.2%) resulted in the low precipitation of Cr-containing precipitates.

### 4.3. Texture Change

The evolution of the macrotexture is illustrated by constant $\varphi_2$ sections of the ODF in Fig. 11(e) and Fig. 11(f). The common recrystallization textures in fcc metals which are the {001} < 100 > cubic texture, {011} < 211 > brass texture, {112} < 111 > copper texture, the {011} < 100 > Goss texture and the {111} < 211 > R texture [65]. In order to reveal further the correlation between DRXed-grains and texture evolution, the EBSD mappings of the DRXed grains at 700 °C and 900 °C (Fig. 11a and b) were analyzed. A threshold value of 2° for grain orientation spread (GOS) was chosen to identify the recrystallized grains [66]. Fig. 11(c) and Fig. 11(e) show the polar diagram and ODF maps of recrystallized grains at 700 °C, respectively. The main texture is {001} < 100 > cubic texture with a maximum intensity of about 9.1. When the temperature is 900 °C (Fig. 11(d) and Fig. 11(f)), the texture is {011} < 100 > Goss texture, and the maximum intensity is about 4.7. It is indicated that the higher deformation temperature makes the texture more random by lowering the texture intensity. This conclusion is consistent with the research of Hu. et al. [67,68].

## 5. Conclusions

Hot deformation tests of the Cu-1.5Ni-1.1Co-0.65Si-0.2Cr alloy were conducted at the deformation temperature ranging from 500 °C to 900 °C and the strain rate ranging from 0.001 $s^{-1}$ to 10 $s^{-1}$. The hot deformation behavior and microstructure were analyzed, and the following conclusions can be drawn:

(1) The flow stress increased with decreased temperature or increased strain rate.

(2) The activation energy $Q$ was determined as 634.45 kJ/mol. The higher activation energy of the Cu-1.5Ni-1.1Co-0.65Si-0.2Cr alloy than pure copper resulted from the precipitation-hardened of $(Ni, Co)_2Si$. The constitutive equation for hot deformation was:

$$\dot{\varepsilon} = e^{78.83}[\sinh(0.0049\sigma)]^{14.98} exp\left(-\frac{634.45}{RT}\right).$$

(3) The precipitates of the Cu-1.5Ni-1.1Co-0.65Si-0.2Cr alloy are mainly disk-shaped and rod-shaped $(Ni, Co)_2Si$, which hinder dislocations and grain boundaries movement, improving the alloy strength.

(4) The dislocation density of the Cu-1.5Ni-1.1Co-0.65Si-0.2Cr alloy is high at low temperature, and with the increase of temperature, the dislocation density is consumed to promote recrystallization. In addition, the number of HAGBs is increased by recrystallization. It is found that the CDRX and DDRX mechanisms are two dominant DRX mechanisms of the Cu-1.5Ni-1.1Co-0.65Si-0.2Cr alloy.

(5) The DRX grains texture of the Cu-1.5Ni-1.1Co-0.65Si-0.2Cr alloy at 700 °C is $\{001\} < 100 >$ cubic texture, which is replaced by the $\{011\} < 100 >$ Goss texture at 900 °C. And it is worth noting that the higher deformation temperature makes the texture more random by lowering the texture intensity.

## Declaration of Competing Interest

The authors declare that they have no known competing financial interests or personal relationships that could have appeared to influence the work reported in this paper.

## Acknowledgements

This work was supported by the Open Cooperation Project of Science and Technology of the Henan Province (182106000018), the Henan University Scientific and Technological Innovation Talent Support Program (18HASTIT024) and the National Natural Science Foundation of China (U1704143).

## References

[1] Q. Lei, S. Li, J.L. Zhu, Z. Xiao, F.F. Zhang, Z. Li, Microstructural evolution phase transition, and physicsproperties of a high strength Cu–Ni–Si–Al alloy, Mater. Charact. 147 (2019) 315–323.

[2] B.J. Wang, Y. Zhang, B.H. Tian, J.C. An, A.A. Volinsky, H.L. Sun, Y. Liu, K.X. Song, Effects of Ce addition on the Cu-Mg-Fe alloy hot deformation behavior, Vacuum 155 (2018) 594–603.

[3] K.M. Liu, Z.K. Huang, X.W. Zhang, D.P. Lu, A. Atrens, H.T. Zhou, Y. Yin, J.M. Yu, W. Guo, Influence of Ag micro-alloying on the thermal stability and ageing characteristics of a Cu–14Fe in-situ composite, Mater. Sci. Eng. A 673 (2016) 1–7.

[4] S.A. Lockyer, F.W. Noble, Precipitate structure in a Cu-Ni-Si alloy, J. Mater. Sci. 29 (1994) 218–226.

[5] Z. Zhao, Y. Zhang, B.H. Tian, Y.L. Jia, Y. Liu, K.X. Song, A.A. Volinsky, Co effects on Cu-Ni-Si alloys microstructure and physical properties, J. Alloys Compd. 797 (2019) 1327–1337.

[6] J. Huang, Z. Xiao, J. Dai, Z. Li, H.Y. Jiamg, W. Wang, X.X. Zhang, Microstructure and properties of a novel Cu–Ni–Co–Si–Mg alloy with super-high strength and conductivity, Mater. Sci. Eng. A 744 (2019) 754–763.

[7] Y. Liu, S. Shao, K.M. Liu, X.J. Yang, D.P. Liu, Microstructure refinement mechanism of Cu–7Cr in situ composites with trace Ag, Mater. Sci. Eng. A 531 (2012) 141–146.

[8] Y.F. Geng, X. Li, H.L. Zhou, Y. Zhang, Y.L. Jia, B.H. Tian, Y. Liu, Alex A. Volinsky, X.H. Zhang, K.X. Song, G.X. Wang, L.H. Li, J.R. Hou, Effect of Ti addition on microstructure evolution and precipitation in Cu-Co-Si alloy during hot deformation, J. Alloys Compd. 842 (2019) 153518.

[9] S.Z. Han, J.H. Gu, J.H. Lee, Z.P. Que, J.H. Shin, S.H. Lim, S.S. Kim, Effect of V addition on hardness and electrical conductivity in Cu-Ni-Si alloys, Met. Mater. Int. 19 (2013) 637–641.

[10] M. Huang, C. Wang, H. Cui, W. Zhang, C. Zhang, Investigation of the structure and properties of AlCrCuFeNiVx high-entropy alloys, Vacuum 173 (2020) 109129.

[11] Y. Wu, Y. Li, J. Lu, S. Tan, F. Jiang, J. Sun, Effects of pre-deformation on precipitation behaviors and properties in Cu-Ni-Si-Cr alloy, Mater. Sci. Eng. A 742 (2019) 501–507.

[12] W. Wang, H.J. Kang, Z.N. Chen, Z.J. Chen, C.L. Zhou, R.G. Li, G.M. Yin, T.M. Wang, Effects of Cr and Zr additions on microstructure and properties of Cu-Ni-Si alloys, Mater. Sci. Eng. A 673 (2016) 378–390.

[13] E. Isidro Gabriel, M.F. Giordana, A.V. Druker, Effect of heat treatment on the microstructure and shape memory behaviour of Fe-Mn-Si-Ni-Cr alloys, Mater. Charact. 155 (2019) 109811.

[14] K.M. Liu, Z.Y. Jiang, J. Zhao, J. Zhou, Z. Chen, D.P. Liu, Effect of directional solidification rate on the microstructure and properties of deformation-processed Cu–7Cr–0.1Ag in situ composites, J. Alloys Compd. 612 (2014) 221–226.

[15] G.S. Peng, K.H. Chen, H.C. Fang, S.Y. Chen, Effect of Cr and Yb additions on microstructure and properties of low copper Al–Zn–Mg–Cu–Zr alloy, Mater. Des. 36 (2012) 279–283.

[16] T.M. Ribeiro, E. Catellan, A. Garcia, C.A. Santos, The effects of Cr addition on microstructure, hardness and tensile properties of as-cast Al–3.8wt.%Cu–(Cr) alloys, J. Mater. Sci. Technol. 9 (2020) 6620–6631.

[17] L.H. Wang, J.W. Li, Z.F. Che, X.T. Wang, H.L. Zhang, J.G. Wang, M.J. Kim, Combining Cr pre-coating and Cr alloying to improve the thermal conductivity of diamond particles reinforced Cu matrix composites, J. Alloys Compd. 749 (2018) 1098–1105.

[18] Y. Liu, Z. Li, Y.X. Jiang, Y. Zhang, The microstructure evolution and properties of a Cu–Cr–Ag alloy during thermal-mechanical treatment, J. Mater. Res. 32 (2017) 1324–1332.

[19] S. Zhang, H. Zhu, L. Zhang, W. Zhang, H. Yang, X. Zeng, Microstructure and properties of high strength and high conductivity Cu-Cr alloy components fabricated by high power selective laser melting, Mater. Lett. 237 (2019) 306–309.

[20] J.Y. Cheng, B.B. Tang, F.X. Yu, B. Shen, Evaluation of nanoscaled precipitates in a Cu–Ni–Si–Cr alloy during aging, J. Alloys Compd. 614 (2014) 189–195 zhang.

[21] K.M. Liu, Z.Y. Jiang, H.T. Hai, D.P. Liu, A. Atrens, Y. Yang, Effect of heat treatment on the microstructure and properties of deformation-processed Cu-7Cr in situ composites, J. Mater. Eng. Perform. 24 (2015) 4340–4345.

[22] Q. Lei, Z. Li, J. Wang, J.M. Xie, X. Chen, S. Li, Y. Gao, L. Li, Hot working behavior of a super high strength Cu–Ni–Si alloy, Mater. Des. 51 (2013) 1104–1109.

[23] J. Chalon, J.D. Guerin, L. Dubar, A. Dubois, E.S. Puchi-Cabrera, Characterization of the hot-working behavior of a Cu-Ni-Si alloy, Mater. Sci. Eng. A 667 (2016) 77–86.

[24] J. Zhang, Q. Wang, D. Chen, Y. Shu, C.P. Wang, G. Chen, Z.D. Zhao, Study of dynamic recrystallization behavior of T2 copper in hot working conditions by experiments and cellular automaton method, J. Alloys Compd. 784 (2019) 1071–1083.

[25] B.J. Wang, Y. Zhang, B.H. Tian, V. Yakouov, J.C. An, A.A. Volinsky, Y. Liu, K.X. Song, L.H. Li, M. Fu, Effects of Ce and Y addition on microstructure evolution and precipitation of Cu-Mg alloy hot deformation, J. Alloys Compd. 781 (2019) 118–130.

[26] M.J. Wang, C.Y. Sun, M.W. Fu, Z.L. Liu, L.Y. Qian, Study on the dynamic recrystallization mechanisms of Inconel 740 superalloy during hot deformation, J. Alloys Compd. 820 (2019) 153325.

[27] Y. Xu, L.X. Hu, T.Q. Deng, L. Ye, Hot deformation behavior and processing map of as-cast AZ61 magnesium alloy, Mater. Sci. Eng. A 559 (2013) 528–533.

[28] Z. Yang, Y.C. Guo, J.P. Li, F. He, F. Xia, M.X. Liang, Plastic deformation and dynamic recrystallization behaviors of Mg–5Gd–4Y–0.5Zn–0.5Zr alloy, Mater. Sci. Eng. A 485 (2008) 487–491.

[29] H.J. Mc Queen, Development of dynamic recrystallization theory, Mater. Sci. Eng. A 387 (2004) 203–208.

[30] A. Galiyev, R. Kaibyshev, G. Gottstein, Correlation of plastic deformation and dynamic recrystallization in magnesium alloy ZK60, Acta Mater. 49 (2001) 1199–1207.

[31] N. Tahreen, D.F. Zhang, F.S. Pan, X.Q. Jiang, D.Y. Li, D.L. Chen, Hot deformation and processing map of an as-extruded Mg-Zn-Mn-Y alloy containing I and W phases, Mater. Des. 87 (2015) 245–255.

[32] X. Chen, Q. Liao, Y.X. Niu, W.T. Jia, Q.C. Le, C.L. Cheng, F.X. Yu, J.Z. Cu, A constitutive relation of AZ80 magnesium alloy during hot deformation based on Arrhenius and Johnson–Cook model, J. Mater. Res. Technol. 8 (2) (2019) 1859–1869.

[33] C.M. Sellars, W.J. McTegart, On the mechanism of hot deformation, Acta Metall. 14 (1966) 1136–1138.

[34] H.D.S. Yong, S.M. Li, R.Q. Hua, Y.L. Run, L. Ping, Developed constitutive models, processing maps and microstructural evolution of Pb-Mg-10Al-0.5B alloy, Mater. Charact. 129 (2017) 353–366.

[35] H. Mirzadeh, J.M. Cabrera, A. Najafizadeh, Modeling and prediction of hot deformation flow curves, Metall. Mater. Trans A 43 (2012) 108–123.

[36] S.S.S. Kumar, T. Raghu, P.P. Bhattacharjee, G.A. Rao, U. Borah, Constitutive modeling for predicting peak stress characteristics during hot deformation of hot isostatically processed nickel-base superalloy, J. Mater. Sci. 50 (2015) 6444–6456.

[37] H. Khodashenas, H. Mirzadeh, M. Malekan, M. Emamy, Constitutive modeling of flow stress during hot deformation of Sn-Al-Zn-Cu-Mg multi-principal-element alloy, Vacuum 170 (2019) 108970.

[38] W.L. Cheng, B. Yang, C.M. Shi, F.W. Li, X.W. Hong, Y. Hui, Hot deformation behavior and workability characteristic of a fine-grained Mg-8Sn-2Zn-2Al alloy with processing map, J. Mater. Sci. Technol. 35 (6) (2019) 1198–1209.

[39] W. Cong, T.L. Yun, L. Tao, J.L. Tian, H.Z. Yu, H. Hua, S.Y. Yuan, Hot compression deformation behavior of Mg-5Zn-3.5Sn-1Mn-0.5Ca-0.5Cu alloy, Mater. Charact. 157 (2019) 109896.

[40] K. Edalati, Z. Horita, Correlations between hardness and atomic bond parameters of pure metals and semi-metals after processing by high-pressure torsion, Scr. Mater.

64 (2011) 161–164.

[41] Y.J. Ban, Y. Zhang, Y.L. Jia, B.H. Tian, A.A. Volinsky, X.H. Zhang, Q.F. Zhang, Y.F. Geng, Y. Liu, X. Li, Effects of Cr addition on the constitutive equation and precipitated phases of copper alloy during hot deformation, Mater. Des. 191 (2020) 108613.

[42] H. Jiang, J. Dong, M. Zhang, Z. Yao, A study on the effect of strain rate on the dynamic recrystallization mechanism of alloy 617B, Metall. Mater. Trans. A 47 (2016) 5071–5087.

[43] L. Hou, J. Hui, Y. Yao, J. Chen, J. Liu, Effects of boron content on microstructure and mechanical properties of AlFeCoNiBx high entropy alloy prepared by vacuum arc melting, Vacuum 164 (2019) 212–218.

[44] J. Yi, Y.L. Jia, Y.Y. Zhao, Z. Xiao, K.J. He, Q. Wang, M.P. Wang, Z. Zhou, Precipitation behavior of Cu-3.0-Ni-0.72 Si alloy, Acta Mater. 166 (2019) 261–270.

[45] K. Toman, The structure of Ni2Si, Acta Crystallogr. 5 (1952) 329–331.

[46] S. Geller, V.M. Wolontis, The crystal structure of Co2Si, Acta Crystallogr. 8 (1955) 83–87.

[47] L. Blaz, E. Evangelista, M. Niewczas, Precipitation effects during hot deformation of a copper alloy, Metall. Mater. Trans. A 25 (1994) 257–266.

[48] A.S.H. Kabir, M. Sanjari, J. Su, I.-H. Jung, S. Yue, Effect of strain-induced precipitation on dynamic recrystallization in Mg-Al-Sn alloys, Mater. Sci. Eng. A 616 (2014) 252–259.

[49] Q.Y. Zhao, F. Yang, R. Torrens, L. Bolzoni, Evaluation of the hot workability and deformation mechanisms for a metastable beta titanium alloy prepared from powder, Mater. Charact. 149 (2019) 226–238.

[50] H. He, Y. Yi, J. Cui, S.Q. Huang, Hot deformation characteristics and processing parameter optimization of 2219 Al alloy using constitutive equation and processing map, Vacuum 160 (2018) 293–302.

[51] K. Huang, R.E. Logé, A review of dynamic recrystallization phenomena in metallic materials, Mater. Des. 111 (2016) 548–574.

[52] S. Wang, J.R. Luo, J.S. Zhang, L.Z. Zhuang, Physically based constitutive analysis and microstructural evolution of AA7050 aluminum alloy during hot compression, Mater. Des. 107 (2016) 277–289.

[53] J. Ren, R. Wang, Y. Feng, C. Peng, Z. Cai, Hot deformation behavior and microstructural evolution of as-quenched 7055 Al alloy fabricated by powder hot extrusion, Mater. Charact. 156 (2019) 109833.

[54] S. Liu, Q. Pan, M. Li, X. Wang, J. Lai, Microstructure evolution and physical-based diffusion constitutive analysis of Al-Mg-Si alloy during hot deformation, Mater. Des. 184 (2019) 108181.

[55] Y.C. Lin, X.H. Zhu, W.Y. Dong, Y.W. Xiao, N. Kotkunde, Effects of deformation parameters and stress triaxiality on the fracture behaviors and microstructural evolution of an Al-Zn-Mg-Cu alloy, J. Alloys Compd. 832 (2020) 154988.

[56] B.C. Xie, B.Y. Zhang, H. Yang, Q. Liu, Y.Q. Ning, Microstructure evolution and underlying mechanisms during the hot deformation of 718Plus superalloy, Mater. Sci. Eng. A 784 (2020) 139334.

[57] Q.H. Zeng, B.F. Luan, Y.H. Wang, X.Y. Zheng, R.P. Liu, K.L. Murty, Q. Liu, Effect of initial orientation on dynamic recrystallization of a zirconium alloy during hot deformation, Mater. Charact. 145 (2018) 444–453.

[58] D. Jia, W. Sun, D.S. Xu, F. Liu, Dynamic recrystallization behavior of GH4169G alloy during hot compressive deformation, J. Mater. Sci. Technol. 35 (2019) 1851–1859.

[59] D.Q. Zhou, X.Q. Xu, H.H. Mao, Y.F. Yan, T.G. Nieh, Z.P. Liu, Plastic flow behaviour in an alumina-forming austenitic stainless steel at elevated temperatures, Mater. Sci. Eng. A 594 (2014) 246–252.

[60] W.C. Xu, X.Z. Jin, W.D. Xiong, X.Q. Zeng, D.B. Shan, Study on hot deformation behavior and workability of squeeze-cast 20 vol%SiCw/6061Al composites using processing map, Mater. Charact. 135 (2017) 154–166.

[61] Y. Li, T.G. Landon, Creep behavior of an Al-6061 metal matrix composite reinforced with alumina particulates, Acta Mater. 45 (1997) 4797–4806.

[62] S.J. Zhu, L.M. Peng, Z.Y. Ma, J. Bi, F.G. Wang, Z.G. Wangm, High temperature creep behavior of SiC whisker-reinforced Al-Fe-V-Si composite, Mater. Sci. Eng. A 215 (1996) 120–124.

[63] S. Aditya, M.J.N.V. Prasad, S.V.S. Narayana Murty, Effect of initial grain size on hot deformation behaviour of Cu-Cr-Zr-Ti alloy, Mater. Charact. 160 (2020) 110112.

[64] W. Wang, Y.G. En, G.H.J.K. Hui, J.C. Zhong, L.Z. Cun, G.L. Ren, M.Y. Guo, M.W. Tong, Correlation between microstructures and mechanical properties of cryorolled Cu-Ni-Si alloys with Cr and Zr alloying, Mater. Charact. 144 (2018) 532–546.

[65] Y.F. Geng, Y. Zhang, K.X. Song, Y.L. Jia, X. Li, Heinz-RolfStock, H.L. Zhou, B.H. Tian, Y. Liu, Alex A. Volinsky, X.H. Zhang, P. Liu, X.H. Chen, Effect of Ce addition on microstructure evolution and precipitation in Cu-Co-Si-Ti alloy during hot deformation, J. Alloys Compd. 842 (2020) 155666.

[66] P. Liu, R. Zhang, Y. Yuan, C.Y. Cui, Y.Z. Zhou, X.F. Sun, Hot deformation behavior and workability of a Ni-Co based superalloy, J. Alloys Compd. 831 (2020) 154618.

[67] K. Hu, Q.Y. Liao, C.Y. Li, Q.C. Le, W.Y. Zhou, C.L. Chen, S.C. Ning, X.R. Chen, F.X. Yu, High ductility induced by un-DRXed grains in a Mg–Zn–Mn–La–Ce alloy, J. Mater. Sci. 54 (2019) 1–16.

[68] C. Haase, L.A. Barrales-Mora, Influence of deformation and annealing twinning on the microstructure and texture evolution of face-centered cubic high-entropy alloys, Acta Mater. 150 (2018) 88–103.